

Helicity-selective Raman scattering from in-plane anisotropic α -MoO₃

Shahzad Akhtar Ali¹, Abdullah Irfan¹, Aishani Mazumder², Sivacarendran Balendhran³, Taimur Ahmed^{2,4,5}, Sumeet Walia² and Ata Ulhaq^{1*}

¹Physics department, SBA School of Science and Engineering,
Lahore University of Management Sciences LUMS, Sector U, DHA, 54792 Lahore, Pakistan

²School of Engineering, RMIT University Melbourne, Australia.

³School of Physics, The University of Melbourne, Victoria, Australia.

⁴Functional Materials and Microsystems Research Group and the Micro Nano Research Facility
RMIT University Melbourne, Australia.

⁵Pak-Austria Fachhochschule: Institute of Applied Sciences and Technology, Haripur, 22620 Pakistan.

[*Corresponding email: ata.haq@lums.edu.pk](mailto:ata.haq@lums.edu.pk)

(Dated: July 22, 2021)

Hyperbolic crystals like α -MoO₃ can support large wavevectors and photon density as compared to the commonly used dielectric crystals, which makes them a highly desirable platform for compact photonic devices. The extreme anisotropy of the dielectric constant in these crystals is intricately linked with the anisotropic character of the phonons, which along with photon confinement leads to the rich Physics of phonon polaritons. However, the chiral nature of phonons in these hyperbolic crystals have not been studied in detail. In this study, we report our observations of helicity selective Raman scattering from flakes of α -MoO₃. Both helicity-preserving and helicity-reversing Raman scattering are observed. We observe that helical selectivity is largely governed by the underlying crystal symmetry. This study shed light on the chiral character of the high symmetry phonons in these hyperbolic crystals. It paves the way for exploiting proposed schemes of coupling chiral phonon modes into propagating surface plasmon polaritons and for compact photonic circuits based on helical polarized light.

I. INTRODUCTION

Layered van der Waal (vW) crystals, hexa-Boron Nitride (hBN) [1-3] and Molybdenum trioxide [4], belong to a relatively new class of two dimensional (2D) crystals, with in-plane permittivity tensor exhibiting extreme anisotropy. Such materials demonstrate hyperbolicity i.e. the permittivity possesses both positive and negative principal parts in the infra-red spectral range [5,6]. Due to the hyperbolic nature, these 2D materials can support very high momentum photon modes with much smaller wavelengths. This makes it possible to fabricate nanometer-scale compact photonic devices [7,8]. Consequently, these materials exhibit very high photon density of states, which makes it possible to use Purcell enhancement in these for photonic devices [9-11].

α -MoO₃ has demonstrated very strong in-plane hyperbolicity [12,13], making it a strong candidate for possible nanophotonic applications, especially those requiring polarization control of photons [14-17]. The hyperbolic nature of the dielectric function in these materials is governed by the high anisotropic character of the phonons in these hyperbolic vW materials [18]. The anisotropy in phonon modes appears due to the hybridization of longitudinal phonons with transverse phonons by quasi-static Coulomb interaction mediated by large momentum photons [3]. Strong confinement of photons in these hyperbolic vW materials makes them an excellent platform for demonstration of polariton effects of excitons and phonons. Indeed, exciton and phonon-polariton (PhP) effects have been observed both in hBN [1,2,19] and MoO₃ [4,20]. Since the optical anisotropy is governed by the Raman anisotropy, therefore the character and details of phonon mediated scattering process from these naturally occurring hyperbolic crystals is crucial.

Phonon band structure of hBN [21] and α -MoO₃ [22-24] have been studied theoretically and experimentally. However, detailed in-plane anisotropic phonon and corresponding Raman studies have only been reported recently [18,25]. Raman scattering is dominated by the phonons near the high symmetry k -points [18]. Polarization character of Raman photons is governed by the symmetry of the underlying crystal phonons, which provide the required energy and angular momentum for the Raman scattering processes [26]. Angular momentum must be conserved during Raman scattering of helical photons and can give important information about the character of phonons. Reversal of photon helicity during the scattering process, for example, indicate the presence of chiral phonons in high symmetry points. Of course, such scattering should be symmetry allowed to occur. High symmetry phonons in two dimensional hexagonal crystals like transition metal dichalcogenides and hBN have shown to have chiral character and hence can support symmetry induced helicity reversal of scattered Raman photon [27]. Some features of

Raman scattering from flakes of α -MoO₃ are still not explored. For example, do the high-symmetry phonons in flakes of non-hexagonal crystals like α -MoO₃ possess chirality? Can the phonon branches in α -MoO₃ support both helicity conserving and helicity reversing Raman scattering processes? Helical selectivity in hexagonal 2D crystals obeys very robust selection rules, so much so that helicity resolved Raman scattering is a more reliable method for symmetry assignment of the mode [28]. Do non hexagonal 2D crystals like α -MoO₃ demonstrate similarly robust helical selection rules for Raman scattering?

In this work, we present results of our detailed Raman investigations on flakes of α -MoO₃. We present in-plane Raman anisotropy of these flakes along with the polarization profile of scattered Raman modes under linear polarized excitation. More importantly, we show in-plane helicity-resolved Raman spectroscopy from flakes of α -MoO₃ under backscattering geometry. We observe clear helical selectivity for the Raman modes. Both helicity-conserved and helicity-switched Raman scattering processes are observed. This suggests the presence of chiral phonons in the α -MoO₃. Most of our results can be explained by the underlying symmetry of the crystal. Furthermore, the helicity of Raman scattered phonons is independent of number of layers for multilayered flakes.

II. EXPERIMENTAL DETAILS

A. Sample

Bulk α -MoO₃ crystals were synthesized via physical vapor deposition. Commercial MoO₃ powder (Sigma-Aldrich) was evaporated in a horizontal tube furnace at 785°C and bulk crystals were deposited at 560 °C. The deposition was carried out in a vacuum environment, with argon as the carrier gas for vapor transport (1 Torr). Subsequently, the bulk crystals were mechanically exfoliated using adhesive tape and thin flakes were transferred on to 300 nm SiO₂ on Si substrates for characterization.

B. Experimental Setup

These flakes were then studied using an in-house assembled micro-Raman setup built in a confocal geometry (see Figure S2 in Appendix B). The setup is fitted with a 532 nm (2.33 eV) single mode laser, which is focused on the sample via an infinity-corrected long working distance 50X objective (Olympus LMPLFLN50X). The back scattered Raman and Rayleigh scattered laser is collected via the same objective. Collection of the Rayleigh scattered laser is suppressed via a 533 nm notch filter (Thorlabs NF533-17). Raman spectrum is detected via an imaging spectrometer Horiba iHR550 fitted with 1200 lines/mm grating. All the measurements presented here are performed at room temperature.

For helicity resolved Raman, laser of a specific helicity are prepared using a linear polarizer and an achromatic $\lambda/4$ retarder (from Bernhard Halle Nachfl. GmbH). Scattered Raman modes are then helically selected via the same $\lambda/4$ retarder. A combination of linear polarizer and an achromatic $\lambda/2$ retarder (Bernhard Halle Nachfl. GmbH) is used to probe the co-polarized and cross-polarized helical polarization plane (see Figure S2 in Supplementary Material).

For Raman anisotropy measurements (see Figure S2(a) in Supplementary Material), the sample was fixed and the incident polarization was rotated with respect to the in-plane crystallographic c axis using a $\lambda/2$ retarder. The detection polarization angle was selected via another $\lambda/2$ retarder and a linear polarizer. The detection polarization is kept parallel to the incident polarization for all measurements here (see Figure S2(c) in Supplementary Material for the setup schematic).

For polarization-resolved detection of Raman modes under linear excitation (see Figure S2(b) in Supplementary Material), the incident linear excitation was kept at a fixed angle with respect to the in-plane crystallographic c axis, while the detection polarization was selected using a linear polarizer and a $\lambda/2$ retarder.

C. Experimental Results and discussion

α -MoO₃ possess octahedral symmetry with D_{16}^{2h} or $Pnma$ space group [25] (see Figure 1b for a depiction of the structure). The primitive unit cell has 16 atoms, which give rise to 45 optical phonon branches and 3 acoustic phonon branches. Group theory analysis suggest 8 A_g , 4 B_{1g} , 8 B_{2g} , and 4 B_{3g} Raman-active modes [18,25].

1. Raman spectroscopy on α -MoO₃

Molybdenum trioxide is a wide bandgap semiconductor with a direct bandgap of 3.0 eV [13,29] and a monolayer thickness of 0.7 nm [30]. The Raman studies reported here are based on laser scattering of energy of 2.33 eV, i. e. below the bandgap. The flakes are oriented such that the crystallographic c and a axes are aligned in-plane (see Fig. 1(b) for reference). The laser is incident at normal angle, therefore, the Raman configuration for these measurements can be represented by $-y(e_i, e_s)y$, where $-y$ and y represents the direction of the incident and scattering laser in the lab frame, while e_i and e_s represent the *in-plane* polarization state of the incident and scattered laser, respectively. Figure 1a shows a typical Raman spectrum, in which 6 distinct Raman modes are readily observed. These modes include 4 A_g modes at 336, 482, 818 and 996 cm⁻¹. The mode at 283 cm⁻¹ has B_{2g}

character (see discussion below), while the mode at 666 cm^{-1} has a B_{3g} character (see discussion in section 3 of supplementary materials for mode designation). These designations are based on previously reported works [18,28,31,32] and helical selection rules for Raman scattering as discussed below. The peak at 519 cm^{-1} corresponds to the Silicon substrate.

2. Raman anisotropy

The in-plane hyperbolic optical response of flakes of MoO_3 is directly related to the in-plane phonon anisotropy. We probe the in-plane Raman anisotropy by analyzing the Raman mode intensity as a function of the relative angle between the incident laser polarization and crystallographic c -axis. We performed a series of anisotropy measurements and compare our results with the previous studies [18,25]. The Raman scattering cross-section of a specific mode directly depends on the $I \propto |e_s \cdot R \cdot e_i|^2$, where e_i and e_s denote the polarization state of the incident and scattered laser. The Raman susceptibility is represented by the Raman tensors, represented here by symbol R . Each element of the tensor $R_{ij}(\gamma)$ represents the corresponding susceptibility of the γ -th Raman active mode in the crystal coordinates near the Brillouin zone boundary. These tensors for the Raman active modes of MoO_3 are:

$$R(A_g) = \begin{pmatrix} a & 0 & 0 \\ 0 & b & 0 \\ 0 & 0 & c \end{pmatrix} \quad R(B_{1g}) = \begin{pmatrix} 0 & d & 0 \\ d & 0 & 0 \\ 0 & 0 & 0 \end{pmatrix} \quad R(B_{2g}) = \begin{pmatrix} 0 & 0 & e \\ 0 & 0 & 0 \\ e & 0 & 0 \end{pmatrix} \quad R(B_{3g}) = \begin{pmatrix} 0 & 0 & 0 \\ 0 & 0 & f \\ 0 & f & 0 \end{pmatrix} \quad (1)$$

The Raman scattering cross section can then be represented in the lab frame as $I \propto |e_s \cdot t^T \cdot R \cdot t \cdot e_i|^2$, where a transformation matrix t converts the crystal coordinates into the lab frame.

$$t = \begin{pmatrix} \cos \theta & 0 & -\sin \theta \\ 0 & 1 & 0 \\ \sin \theta & 0 & \cos \theta \end{pmatrix} \quad (2)$$

The angle θ is the angle between the crystallographic c axis and z axis of the lab frame. The crystallographic y axis coincides with that of the lab frame. The intensities of the Raman active modes can then be written as

$$I(A_g) \propto \left| \begin{pmatrix} 1 \\ 0 \\ 0 \end{pmatrix}^T \begin{pmatrix} \cos \theta & 0 & -\sin \theta \\ 0 & 1 & 0 \\ \sin \theta & 0 & \cos \theta \end{pmatrix}^T R(A_g) \begin{pmatrix} \cos \theta & 0 & -\sin \theta \\ 0 & 1 & 0 \\ \sin \theta & 0 & \cos \theta \end{pmatrix} \begin{pmatrix} 1 \\ 0 \\ 0 \end{pmatrix} \right|^2 \quad (3)$$

$$I(A_g) \propto |c(\cos \theta)^2 + a(\sin \theta)^2|^2 \quad (4)$$

Similarly,

$$I(B_{2g}) \propto |e \sin 2\theta|^2 \quad (5)$$

$$I(B_{1g}) = I(B_{3g}) = 0 \quad (6)$$

According to Raman tensors, only the A_g and B_{2g} modes should be observable. Figure 2 depicts the experimental results of our Raman anisotropy measurements. The data is extracted from Raman studies where the angle between the crystal c axis and incident polarization is gradually changed while the polarization of the incident and detection arm of the setup are parallel. The results clearly show the in-plane anisotropy. The A_g modes at 817 and 992 cm^{-1} have dominant Raman scattering with incident laser polarization along the c -axis ($|c| > |a|$). The A_g mode at 364 cm^{-1} is strongly polarized along the a -axis ($|c| \ll |a|$). These observations agree with the previously reported Raman anisotropy studies [18,25]. However, unlike these studies, the A_g mode at 336 cm^{-1} has maxima both along 0° and 90° . Fitting using Eq. (4) implies $|c| \sim |a|$. For the B_{2g} mode at 283 cm^{-1} , the maxima of the intensity occurs at $+45^\circ$, $+135^\circ$ and so on. Unlike that of A_g mode, the polarization of B_{2g} is aligned along the diagonal of the a - c plane.

To further emphasize the difference in the A_g and B_{2g} modes, we demonstrate the polarization analysis of these modes under constant linear excitation. The linear polarization of incident laser is aligned along the in-plane c -axis and Raman scattering is detected as a function of angle between the detection polarization and the crystal c -axis. The resulting normalized Raman mode intensities of three A_g modes (at 336, 817 and 992 cm^{-1}) and a B_{2g} mode (at 284 cm^{-1}) is plotted in Figure 3. All the scattered Raman modes are linearly polarized. However, the A_g modes have polarization predominantly along the c -axis (or parallel to incident polarization), while the B_{2g} mode has polarization along the diagonal of the a - c plane (or rotated by $\pi/4$ with respect to incident polarization).

3. Helicity-resolved Raman

Recent studies on two dimensional semiconductors have clearly revealed robust selection rules for helicity-resolved Raman scattering [28]. Interestingly, apart from momentum conserving helical Raman scattering, clear signatures of helically switched Raman scattering was reported [28]. Such large momentum transfer was initially attributed to mixing of s - and p -orbitals in the conduction band at high symmetry points along with the wave vector dependent Berry curvature. Later studies clearly attributed these processes to the chiral nature of the phonons at high symmetry point in hexagonal two-dimensional van der Waal crystals [27]. However, such helical selectivity of the Raman modes in biaxial hyperbolic crystals like α - MoO_3 has yet to be reported.

A 2.33 eV laser of a specific helicity is back scattered from the sample. A $\lambda/4$ plate project the helical polarization of the scattered into a plane of co- and cross-polarized polarization along the propagation direction. The co-polarized component refers to the detected Raman with the same helicity as the incident laser while the cross-polarized component represents the detection of reversed helical polarization. A set of $\lambda/2$ and linear polarizer is used for helicity selective detection.

Considering the incident laser along the y axis (lab frame as well as the crystal coordinates), the scattered intensities for the Raman active modes under $\sigma+$ incident laser is given as:

$$I(A_g)_{co} \propto \left| \begin{pmatrix} 1 \\ 0 \\ i \end{pmatrix}^T R(A_g) \begin{pmatrix} 1 \\ 0 \\ i \end{pmatrix} \right|^2 = |a + c|^2 \quad (7)$$

$$I(A_g)_{cross} \propto \left| \begin{pmatrix} 1 \\ 0 \\ -i \end{pmatrix}^T R(A_g) \begin{pmatrix} 1 \\ 0 \\ i \end{pmatrix} \right|^2 = |a - c|^2 \quad (8)$$

$$I(B_{2g})_{co} \propto \left| \begin{pmatrix} 1 \\ 0 \\ i \end{pmatrix}^T R(B_{2g}) \begin{pmatrix} 1 \\ 0 \\ i \end{pmatrix} \right|^2 = 0 \quad (9)$$

$$I(B_{2g})_{cross} \propto \left| \begin{pmatrix} 1 \\ 0 \\ -i \end{pmatrix}^T R(B_{2g}) \begin{pmatrix} 1 \\ 0 \\ i \end{pmatrix} \right|^2 = 4|e|^2 \quad (10)$$

$$I(B_{1g})_{cross} = I(B_{1g})_{co} = 0 = I(B_{3g})_{co} = I(B_{3g})_{co} \quad (11)$$

Using these calculations, only A_g and B_{2g} modes should be observed under helical excitation. The A_g mode has weaker selection rule for scattering as compared to B_{2g} , which should strictly have cross-polarized character.

Figure 4 shows helicity-resolved Raman spectra of α - MoO_3 flake (of thickness 140 nm) under $\sigma+$ excitation. Almost complete switching off of the Raman mode in the co-polarized spectrum ($\sigma+$ detection: green line) and the cross-polarized spectrum ($\sigma-$ detection: orange line) is an indicator of the helical selectivity of the Raman modes. The A_g modes at 336, 817 and 992 cm^{-1} are dominantly co-polarized, however the degree of helical selectivity is higher for the mode at 336 cm^{-1} (vanishingly small $|a - c|^2$) and low for the 817 cm^{-1} ($|a - c|^2 > 0$). The B_{2g} at 283 cm^{-1} as expected has vanishingly small co-polarized intensity as compared to the cross-polarized intensity, as predicted from the Raman tensor. However, the B_{3g} at 666 cm^{-1} has a non-vanishing intensity under helical excitation, contrary to the predictions. Surprisingly, it shows a dominant cross-polarized character as well. We attribute this to the non-normal part of the incident as the laser is focused onto the flake surface (see discussion in section 3 of Supplementary Material).

These measurements were repeated and verified on several flakes of α - MoO_3 with thickness ranging from 140 nm to 300 nm (thicknesses verified using AFM scans: check Supplementary Material). The helically selective scattering of the modes is similar under $\sigma-$ excitation as well.

To further explore the helical selectivity of the Raman modes, we performed a full polarization angle dependent analysis of the Raman detection in the two-dimensional polarization plane formed by the co- and cross-polarized helical components (see Figure 5f and Figure S2(c) in Appendix B). Polar plots of the normalized Raman signal for 5 different modes are shown in Figure 5(a)-(e). All the A_g modes have highest intensities along the co-polarized axis. The cross-polarized component for the 336 cm^{-1} mode is $\sim 12\%$ of the maximum intensity, while that of 992 cm^{-1} is 20% and that of 817 cm^{-1} mode has a large cross-polarized component of 27%. Both the B_{2g} and B_{3g} modes are predominantly cross-polarized, which implies that the crystal imparts an angular momentum to the photon thereby switching the helicity of the scattered photons. B_{2g} has a higher degree of polarization switching (less than 1% of co-polarized scattering) as compared to the B_{3g} mode ($\sim 8\%$ of co-polarized Raman scattering). Scattering of B_{2g} Raman mode involves almost complete reversal of the helicity of the incident photon. These results point toward the chiral character of the orthorhombic α - MoO_3 crystal, which requires a detailed theoretical explanation.

Helical selectivity of Raman mode in hexagonal 2D crystals has been used as a robust indicator for the symmetry designation of a Raman mode [27]. Equations (9)-(11) shows that B_{2g} and B_{3g} Raman modes of α - MoO_3 have clear helical selectivity. This selectivity can be used for reliable mode identification, as well crystal plane identification. For example, relative intensity difference between the B_{2g} mode at 283 cm^{-1} and B_{3g} mode at 666 cm^{-1} indicates that the plane of the MoO_3 flake is defined by the a - c crystal axes (see discussion in section 3 of Supplementary Material). The α - MoO_3 Raman mode around 283 cm^{-1} is designated as a B_{2g} mode in Ref. [25], and B_{1g} mode in Ref. [18]. From Fig. 5(d), this particular mode has predominantly a cross-polarized character. Additionally, it has higher intensity than the helicity forbidden B_{3g} mode at 666 cm^{-1} (see Figure. 4). Therefore, we assign B_{2g} representation to the 283 cm^{-1} mode. Helicity resolved Raman, therefore provides an additional tool for correct symmetry-based designation of the Raman modes.

III CONCLUSIONS

Presence of clear helicity selection in Raman scattering, especially the almost complete helicity switching under Raman scattering, from α - MoO_3 points to a strong phonon chirality around the high symmetry points in Brillouin (phonon scattering is dominated by phonons near the high symmetry points). The helical selectivity largely agrees with the symmetry-based Raman tensors, however a detailed theoretical explanation of the chirality of phonon bands in α - MoO_3 is needed.

The hyperbolic nature of flakes of α - MoO_3 makes them ideal candidates for nano-photonics applications apart from the highly rich Physics of in-plane anisotropic phonon polariton. The chiral nature of the highly anisotropic phonons in this material system can play a crucial role in proposals which combine this hyperbolicity with spin-orbit coupling resulting in novel surface plasmon modes [33]. Especially in schemes which rely on coupling of chiral Raman modes into propagating surface plasmon polaritons [34]. Understanding of the chiral nature of the phononic bands can be vital for photonic circuits involving helical metamaterials [35,36].

Acknowledgements

S. A. A. acknowledges PhD funding from SBASSE LUMS. A. U. acknowledge funding from LUMS via FIF-523.

Data Availability

The data that support the findings of this study are available from the corresponding author upon reasonable request.

References

- [1] Caldwell, J. D. *et al.*, "Sub-diffractive volume-confined polaritons in the natural hyperbolic material hexagonal boron nitride" *Nature communications*, 5(1), 1-9 (2014).
- [2] Dai, Siyuan *et al.*, "Hyperbolic phonon polaritons in suspended hexagonal boron nitride". *Nano letters* 19, no. 2, 1009-1014 (2018).
- [3] Low, Tony *et al.*, "Polaritons in layered two-dimensional materials", *Nature materials*, 16, 2, 182-194, (2017)
- [4] Ma, Weiliang, *et al.* "In-plane anisotropic and ultra-low loss polaritons in a natural van der Waals crystal". *Nature* 562 (7728), 557-562 (2018).
- [5] Poddubny, A., Iorsh, I., Belov, P., & Kivshar, Y. (2013). Hyperbolic metamaterials. *Nature photonics*, 7(12), 948-957.
- [6] Guo, Zhiwei, Haitao Jiang, and Hong Chen. "Hyperbolic metamaterials: From dispersion manipulation to applications." *Journal of Applied Physics* 127.7 (2020): 071101.
- [7] Zhukovsky, Sergei V., et al. "From surface to volume plasmons in hyperbolic metamaterials: general existence conditions for bulk high-k waves in metal-dielectric and graphene-dielectric multilayers." *Physical Review B* 90.15 (2014): 155429.
- [8] Takayama, Osamu, and Andrei V. Lavrinenko. "Optics with hyperbolic materials." *JOSA B* 36.8 (2019): F38-F48.
- [9] Noginov, M. A., et al. "Controlling spontaneous emission with metamaterials." *Optics letters* 35.11 (2010): 1863-1865.
- [10] Tumkur, T., et al. "Control of spontaneous emission in a volume of functionalized hyperbolic metamaterial." *Applied Physics Letters* 99.15 (2011): 151115.
- [11] Krishnamoorthy, Harish NS, et al. "Topological transitions in metamaterials." *Science* 336.6078 (2012): 205-209.
- [12] Zheng, Zebo, et al. "A mid-infrared biaxial hyperbolic van der Waals crystal." *Science advances* 5.5 (2019): eaav8690.
- [13] Balendhran, Sivacarendran, et al. "Two-dimensional molybdenum trioxide and dichalcogenides." *Advanced Functional Materials* 23.32 (2013): 3952-3970.
- [14] Folland, Thomas G., and Joshua D. Caldwell. "Precise control of infrared polarization using crystal vibrations." *Nature* 562, 499-501 (2018).
- [15] Dixit, Saurabh et al., "Mid infrared polarization engineering via sub-wavelength biaxial hyperbolic van der Waals crystals", *Scientific Reports* 11, 6612 (2021)
- [16] Li, Peining, et al. "Infrared hyperbolic metasurface based on nanostructured van der Waals materials." *Science* 359.6378 (2018): 892-896.
- [17] Nicholls, Luke H., et al. "Ultrafast synthesis and switching of light polarization in nonlinear anisotropic metamaterials." *Nature Photonics* 11.10 (2017): 628-633.
- [18] Wen, Muqian et al., "In-Plane Anisotropic Raman Spectroscopy of van der Waals α -MoO₃", *The Journal of Physical Chemistry C*, (2020).
- [19] Woessner, Achim, et al. "Highly confined low-loss plasmons in graphene–boron nitride heterostructures". *Nature materials* 14 (4), 421-425 (2015).
- [20] Zheng, Zebo et al., "Highly confined and tunable hyperbolic phonon polaritons in van der Waals semiconducting transition metal oxides", *Advanced Material* 30, 13, 1705318 (2018).
- [21] Michel, K. H., and B. Verberck. "Phonon dispersions and piezoelectricity in bulk and multilayers of hexagonal boron nitride." *Physical Review B* 83.11 (2011): 115328.
- [22] Lee, S. H. et al., "Raman spectroscopic studies of electrochromic α -MoO₃ thin films". *Solid State Ionics*, 147(1-2), 129-133 (2002).
- [23] Camacho-López, M. A. et al., "Micro-Raman study of the m-MoO₂ to α -MoO₃ transformation induced by cw-laser irradiation" *Optical Materials*, 33(3), 480-484 (2011).
- [24] Spevack, P. A., and N. S. McIntyre. "Thermal reduction of molybdenum trioxide", *The Journal of Physical Chemistry* 96, (22), 9029-9035 (1992).

- [25] Zheng, Binjie, *et al.* "Centimeter-sized 2D α -MoO₃ single crystal: growth, Raman anisotropy, and optoelectronic properties." *2D Materials* 5.4, 045011 (2018).
- [26] Powell, Richard C. *Symmetry, group theory, and the physical properties of crystals*. Vol. 824. New York: Springer, 2010.
- [27] Zhang, Lifa, and Qian Niu. "Chiral phonons at high-symmetry points in monolayer hexagonal lattices", *Physical review letters* 115, 115502 (2015).
- [28] Chen, S. Y., Zheng, C., Fuhrer, M. S., & Yan, J. "Helicity-resolved Raman scattering of MoS₂, MoSe₂, WS₂, and WSe₂ atomic layers.", *Nano letters*, 15(4), 2526-2532 (2015).
- [29] Vos, Martijn FJ, et al. "Atomic layer deposition of molybdenum oxide from (N t Bu) 2 (NMe2) 2Mo and O2 plasma." *Journal of Vacuum Science & Technology A: Vacuum, Surfaces, and Films* 34.1 (2016): 01A103.
- [30] Cai, Lili, et al. "Rapid flame synthesis of atomically thin MoO₃ down to monolayer thickness for effective hole doping of WSe₂." *Nano letters* 17.6 (2017): 3854-3861.
- [31] Syrbu, N. N., and I. G. Stamov. "The superposition of the lattice radiation and reflectivity spectra of MoO₃ and PbMoO₄ crystals." *Crystal Research and Technology* 29.1: 133-148 (1994).
- [32] Eda, Kazuo. "Raman spectra of hydrogen molybdenum bronze, H_{0.30}MoO₃." *Journal of Solid State Chemistry* 98.2: 350-357 (1992).
- [33] Nemilentsau, Andrei, *et al.* "Switchable and unidirectional plasmonic beacons in hyperbolic two-dimensional materials." *Physical Review B* 99.20 (2019): 201405.
- [34] Guo, Quanbing, et al. "Routing a chiral Raman signal based on spin-orbit interaction of light." *Physical review letters* 123.18 (2019): 183903.
- [35] Kilic, Ufuk, et al. "Broadband enhanced chirality with tunable response in hybrid plasmonic helical metamaterials." *Advanced Functional Materials* 31.20 (2021): 2010329.
- [36] Kaschke, Johannes, and Martin Wegener. "Optical and infrared helical metamaterials." *Nanophotonics* 5.4 (2016): 510-523.

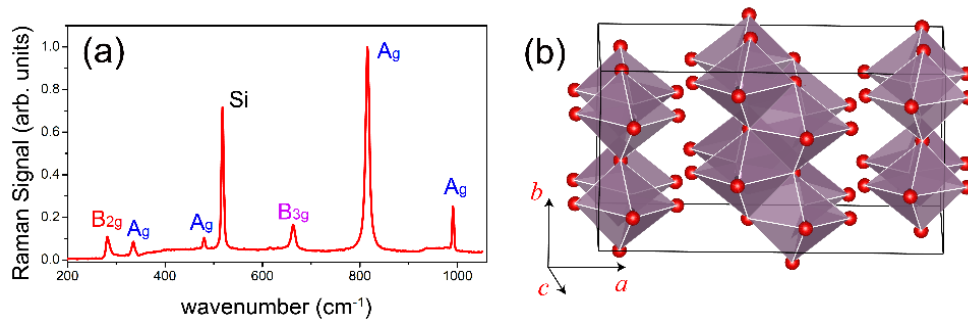


Figure 1: (a) Raman spectrum obtained via scattering of 2.33 eV laser from MoO₃ flake. Excitation power is kept at 1.5 mW and the temperature at 25 °C. The symmetry-based identification of each peak is indicated. (b) Crystal structure of MoO₃. The red spheres represent O atoms while the Mo atoms are enclosed at the center of the octahedrons. Plane surfaces define the orthorhombic structures. Crystallographic axes are identified.

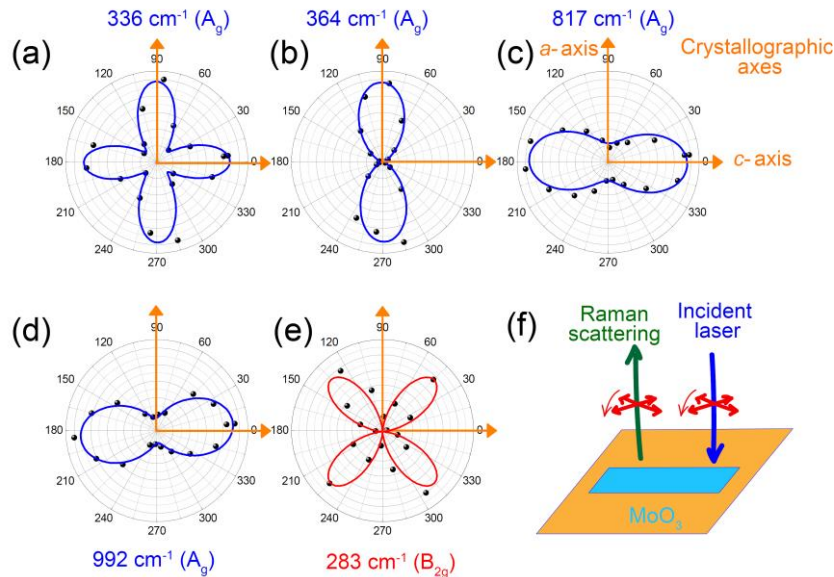


Figure 2: (a)-(e) Raman mode intensity as a function of angle between the incident polarization and crystal axis for 5 selective Raman modes of MoO₃. These include 4 A_g modes and one B_{1g} mode at 283 cm⁻¹. (f) A sketch representing the experimental scheme. Linear polarizer laser is incident while the scattered Raman of a selected polarization is detected. Both the incident laser and the detection polarization are gradually changed to probe the Raman anisotropy of the crystal. It made sure that the incident and detection polarization are always parallel to each other. This is equivalent to rotation of the in-plane crystal axes with respect to a fixed incident laser. The setup can be represented a $-\chi(\cos \theta, \sin \theta)x$.

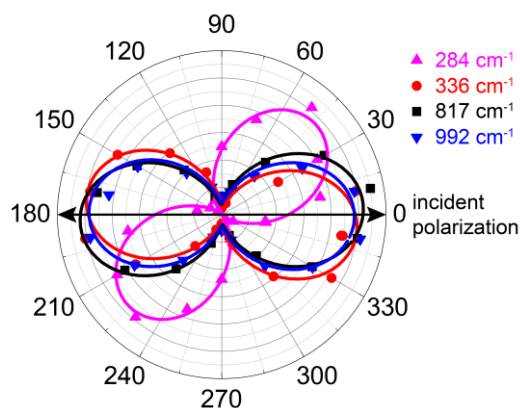


Figure 3: Polarization resolved Raman scattering from MoO₃ flakes. Polar plots of normalized Raman A_g modes at 336 (red), 817 (black) and 992 cm^{-1} (blue) and the B_{2g} mode at 284 cm^{-1} (magenta). Points represent experimental data while the solid lines are theoretical fit to the data using the Raman tensor.

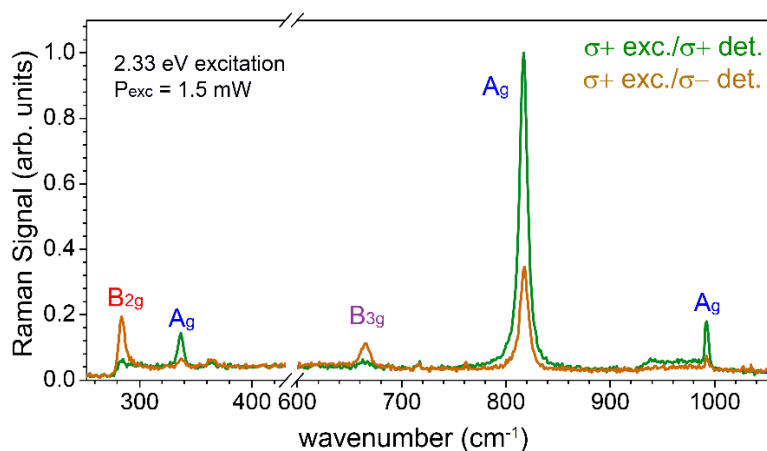


Figure 4: Helicity resolved Raman spectra from a MoO₃ flake. The flake is excited by a $\sigma+$ laser. The green spectrum shows the co-polarized or $\sigma+$ polarized part of the scattered Raman, while the orange one shows the spectrum of the cross-polarized or $\sigma-$ scattered Raman. The experimental configuration can be represented as $-\gamma(\sigma+, \sigma+)y$ for the co-polarized detection while $-\gamma(\sigma+, \sigma-)y$ for the cross-polarized configuration. The Raman peak from Silicon is not shown, for clear visualization of the MoO₃ Raman modes.

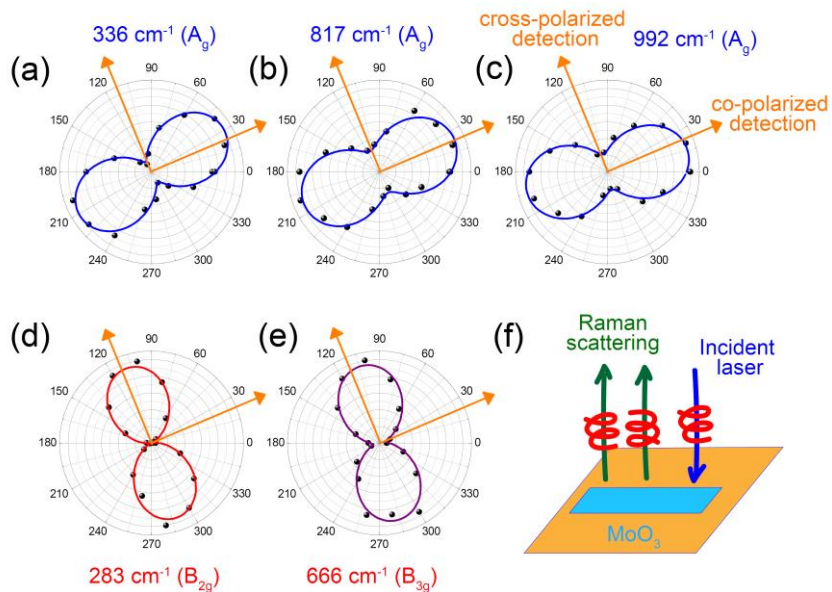


Figure 5: (a)-(e) Normalized Raman mode intensity as a function of polarization selected angle in detection plane, defined by the co- and cross-polarized helical components of the scattered laser. Black dots represent experimental results while solid lines represent the fits extracted from the corresponding Raman tensor. Blue solid line represents fitting of A_g mode, red solid line is the fit to the B_{1g} mode while purple line fit the intensity of the B_{3g} mode. The orange lines show the angles corresponding to the detection polarization angles at which the detected Rayleigh scattering is maximum (co-polarized) or minimum (cross-polarized). (f) A figure representing the experimental scheme. Circular polarized laser of a specific helicity is incident while the scattered Raman of a selected helical polarization is detected. see Figure S2(c) in Supplementary Material for detailed setup.

Supplementary Material: Helicity-selective Raman scattering from in-plane anisotropic α - MoO_3

1. Atomic Force Microscopy Scan of MoO_3 flakes

Atomic force microscopy (AFM) scans of the typical MoO_3 flakes reported in this study are shown in Figure S1. These flakes have thicknesses of 140, 200 and 300 nm, which implies that in this study we are not dealing with a few layer flakes, but rather multilayered.

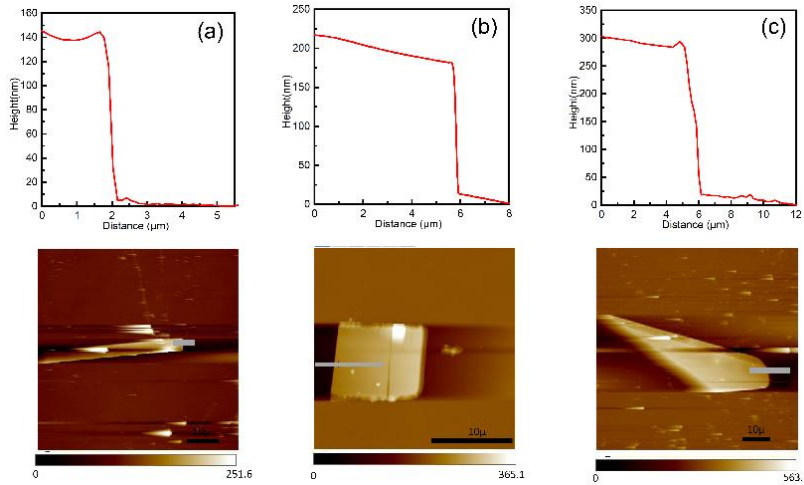


Figure S1: AFM scans on three MoO_3 flakes. The lower panel show the real space images of the flake. The upper panel show the corresponding line scans along the grey line depicting the height of the flakes.

2. Experimental Setup

A 532 nm (2.33 eV) laser is focused on the sample using a 50X long working distance (LWD) objective with a numerical aperture of 0.55. The scattered light is collected via the same objective (confocal setup) and fed into an imaging spectrometer. The laser is filtered out using a notch filter in the detection arm. Various optical polarization components

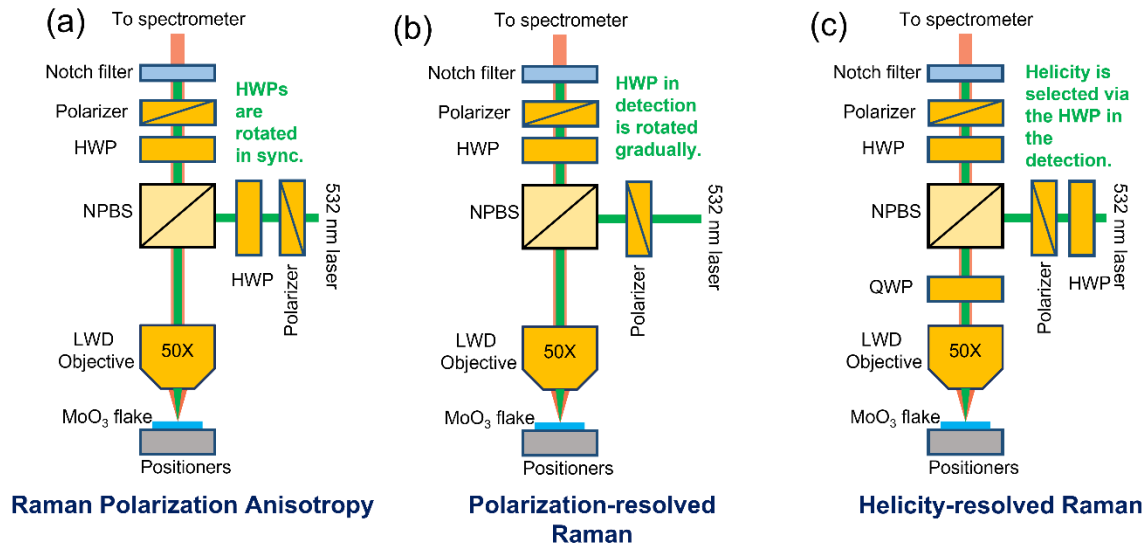


Figure S2: A detailed sketch of the experimental setup for the three different Raman studies discussed in this study. (a) Experimental configuration for measuring the in-plane crystal anisotropy of the Raman modes. The sample is stationary while the polarization of the incident and detection arm are varied parallel to each other using half wave plates (HWP). (b) Setup for measuring the polarization state of the scattered Raman. A fixed polarizer in the incident arm defines the incident linear polarization while Raman spectra are measured as a function of the HWP crystal angle with the incident polarization. (c) Circular polarization laser of a specific helicity is prepared by introducing a quarter wave plate (QWP) below the non-polarizing beam splitter (NPBS). The scattered laser is converted back to linear polarization using the same QWP. A, HWP and a linear polarizer in the detection path then select a particular helicity component for detection.

3. Raman helicity selectivity and sample orientation

Recent experimental studies on α -MoO₃ flakes have reported flakes to be in the crystallographic a - c plane [18] or b - c plane [25]. In this study, we used selection rules for Raman scattering to determine the flakes orientation. As mentioned in the main text, Raman scattering intensity depends on $I \propto |e_s \cdot R \cdot e_i|^2$. The values of $|e_s \cdot R \cdot e_i|^2$ for different combinations of the helical incident and scattered laser is shown in the Table S1. We present data for the cases when the plane of the flake is defined by the crystallographic a - c axes and b - c axes. Apart from the intensity of A_g , the modes B_{2g} and B_{3g} have clear selection rules for both possible orientations of the flakes. Raman scattering of B_{2g} mode is absent in in-plane b - c flake orientation, while the B_{3g} mode is absent in a - c mode. Comparing these with our experimental data shown in Figure 4 of the main text. The B_{2g} mode at 286 cm⁻¹ has higher intensity as compared with the B_{3g} mode at 666 cm⁻¹. We infer that the flake is oriented in a - c crystallographic plane. The B_{3g} is not completely absent because the incident laser is in the form of a focused beam, so a non-negligible part of the incident beam is incident at non-normal angle on the flake surface. Both the B_{2g} and B_{3g} modes have cross-polarized character as predicted from the data in Table S1.

	Flake with in-plane a - c crystal axes				Flake with in-plane b - c crystal axes			
Excitation	$\sigma +$	$\sigma +$	$\sigma -$	$\sigma -$	$\sigma +$	$\sigma +$	$\sigma -$	$\sigma -$
Detection	$\sigma +$	$\sigma -$	$\sigma -$	$\sigma +$	$\sigma +$	$\sigma -$	$\sigma -$	$\sigma +$
A_g	$ a + c ^2$	$ a - c ^2$	$ a + c ^2$	$ a - c ^2$	$ b + c ^2$	$ b - c ^2$	$ b + c ^2$	$ b - c ^2$
B_{1g}	0	0	0	0	0	0	0	0
B_{2g}	0	$4 e ^2$	0	$4 e ^2$	0	0	0	0
B_{3g}	0	0	0	0	0	$4 f ^2$	0	$4 f ^2$

Table S1: Table showing the $|e_s \cdot R \cdot e_i|^2$ for helical incident beam and helicity resolved detection. These values are shown for two configurations: left side of the table represent calculations for the case when the surface of the flake is defined by the crystallographic a - c plane and the right side of the table represents the case when the surface of the flake is in the crystallographic b - c plane.